J Wood Sci (2018) 64:40–51
DOI 10.1007/s10086-017-1669-5

ORIGINAL ARTICLE

Cyclic behavior of Chinese ancient wooden frame with mortise–tenon joints: friction constitutive model and finite element modelling

Qifang Xie[1] · Lipeng Zhang[1] · Shuang Li[2] · Weijian Zhou[3] · Long Wang[1]

Received: 26 April 2017 / Accepted: 17 September 2017 / Published online: 26 October 2017
© The Japan Wood Research Society 2017

Abstract The beams and columns in Chinese ancient wooden buildings were connected with mortise–tenon joints, which are semi-rigid due to the friction and squeezing deformation between mortise and tenon. In this paper, a friction constitutive model for the friction behavior between mortise and tenon was proposed based on the modern frictional theory. A series of surface topography and hardness tests were conducted to obtain some parameters used in the friction constitutive model. A finite element (FE) model of a Chinese ancient wooden frame with mortise–tenon joints under reversed cyclic loading was performed based on the proposed friction constitutive model, and a FE model using a constant friction coefficient was also carried out. Experimental results were used to validate the results modeled by the two models, and better agreement of the proposed model was observed.

Keywords Chinese ancient wooden frames · Mortise–tenon joints · Friction constitutive model · Surface topography and hardness tests · Reversed cyclic loading · Finite element simulation

✉ Qifang Xie
nacy.xie@163.com

Lipeng Zhang
lpgzhang@163.com

Shuang Li
leeshuang@163.com

Weijian Zhou
ZWeijian90@163.com

Long Wang
king_dragon0808@126.com

[1] School of Civil Engineering, Xi'an University of Architecture and Technology, No. 13, Yanta Road, Xi'an 710055, Shaanxi, People's Republic of China

[2] Wuhan China Engineering Science and Technology Limited Company, Wuhan 430000, Hubei, People's Republic of China

[3] Xi'an Qiyu Architectural Design Consulting Limited Company, Xi'an 710000, Shaanxi, People's Republic of China

Introduction

In China, there are many ancient timber buildings [1, 2]. The wooden frameworks provide the using spaces and constitute the load-bearing skeletons. The typical feature of the ancient timber frames in China lies in the natural connection mode of the joints without a metal nail or bolt. These connections mainly include the straight tenon joints (Fig. 1a) and the dovetail joints (Fig. 1b). The straight tenon joint is formed by inserting the tenon at the end of a beam into the mortise opened in a column from the side surface of a column. The mortise used to contain the dovetail tenon must be opened at the top end of a column to ensure that the tenon can be embedded into mortise easily. Frames connected with such joints are typical of semi-rigid characteristics.

Traditionally, many researches about the current situation and structural properties of the ancient timber buildings in China were conducted [3]. The first published book in Song Dynasty by Li [4] is mainly on the construction of timber structures. Ma [5] summarized the construction modes and structural characteristics of ancient Chinese timber architectures. Wang [6] systematically researched the transfer mechanism of vertical load in ancient Chinese timber structures using the structural mechanical theory, which was a relatively earlier research work on the mechanical properties in this field.

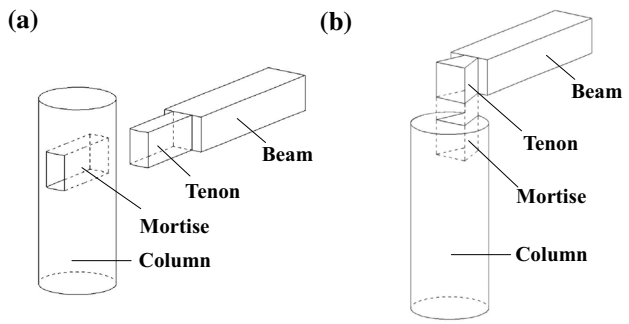

Fig. 1 Joints in Chinese ancient timber buildings. **a** Straight tenon joint; **b** Dovetail joint

In recent years, some achievements about traditional timber frames and mortise and tenon joints have been obtained [7]. Related test results showed significant nonlinearity and inelasticity in the load–displacement curves and the moment–rotation relationships under both static and cyclic lateral load [2, 8–10]. Many research works about the stiffness properties of the mortise and tenon joints were conducted as well [11]. For example, Pan et al. [12] and Xie et al. [13] discussed the mechanical mechanism of the straight tenon joints and dovetail joints, respectively. Wood shrinkage or loading history induced gap at the mortise and tenon joint was researched by Chang et al. [14, 15], and Ogawa et al. [16] to investigate the influence of such insufficient contact on the mechanical performance of the joints. Despite so many research about the wooden frames and the associated mortise and tenon joints, they all regarding the friction coefficient between mortise and tenon as a constant, failing to model the contact behavior efficiently and reveal the corresponding frictional mechanism.

In this paper, a friction constitutive model that can be used to define the contact state and relative slip rate dependent tangential contact behavior between the mortise and tenon was proposed, so as to model the cyclic behavior of Chinese ancient wooden frame with mortise–tenon joints more exactly. A finite element (FE) model of a Chinese ancient wooden frame with mortise–tenon joints under reversed cyclic loading was performed based on the proposed friction constitutive model, and a FE model using a constant friction coefficient was carried out as well.

Mechanical mechanism of wooden frame under lateral load

The test frame (Fig. 2a) is supported by the two steel-rotating supports; the two joints are connected together through four steel bars at the same height as the beam to keep the consistency of their deformation; correspondingly, the lateral load is applied through the horizontal actuator. As for

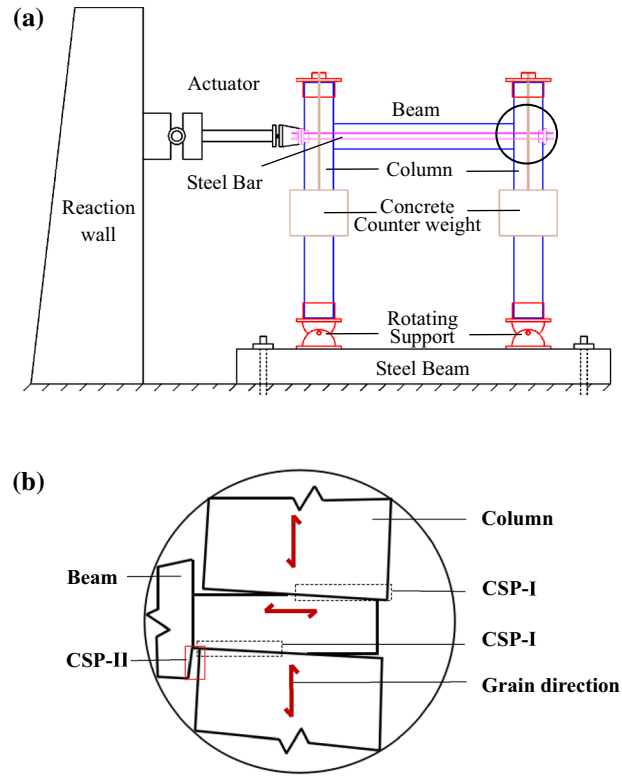

Fig. 2 Friction mechanism between mortise and tenon. **a** Wooden frame with loading setup; **b** detailed drawing of the contact surface pairs of mortise and tenon

using of steel beam to restrict the columns, it eliminates the relative sliding of the whole frame to ensure that the test results can effectively reflect the work property of the beam column joint.

With the lateral load applied on the column (Fig. 2a) gradually, the distance between the top and bottom surfaces of the mortise in the column is getting increasingly close with the top and bottom surfaces of the tenon. The forces that hinder the relative displacement of the mortise and tenon are gradually arising. When the mentioned surfaces are in contact, they start to transfer the occurred normal stress and tangential stress between the mortise and tenon. The interaction conditions of the joint during the pulling-out of the tenon from the mortise are complicated and parts of the contact surface pairs (CSP) can be clearly seen from Fig. 2b. The I type CSP (CSP-I) is the most direct contact surface, which represents the friction area between the transverse section of the mortise and the tangential section of the tenon. CSP-II, another contact surface existing in the joint area, represents the friction area between the transverse section of the beam and the tangential section of the column. CSP-III represents the lateral friction surface pair between the mortise and tenon, the friction between the tangential section of the mortise and the tangential section of the tenon,

which cannot be directly seen from Fig. 2b. Overall, the friction mechanism of the mortise and tenon can fully be reflected by the friction behavior between transverse and tangential sections as well as the transverse and transverse sections of wood. The corresponding mechanical parameters in the following established theoretical model are equally related with the mentioned wood surfaces.

Friction constitutive model between mortise and tenon

Friction mechanism between mortise and tenon

The surfaces of the mortise and tenon are very rough after they are artificially sawed from logs. The contact between the two components' surfaces mainly occur on the asperities peaks on the rough surfaces, being called discontinuous contact or discrete contact, as shown in Fig. 3a. A more detailed schematic of 2D contact morphology in section ABCD was given in Fig. 3b. Under vertical load, the pressure at different contact points takes different values due to their various heights. Plastic deformation usually happens at those peaks of asperities with higher pressure, such as G and H in Fig. 3b. Under such condition, adhesion force will correspondingly arise. The force needed to overcome the adhesion force is regarded as the adhesion component of friction force, without which the relative sliding will not happen between the two rough surfaces. On the other hand, because the hardness of mortise surface is higher than the tenon surface, the former will plough the letter and leave a gully. Seen from the mesoscale, the harder asperity M on the mortise surface will plough the asperity N on the tenon surface with the former's sliding. The force that occurs on the softer surface to resist the ploughing tendency, constitutes the furrow component of the friction force. Therefore, the total friction between two contact rough surfaces consists of both the adhesion component and the furrow component.

Basic assumption

To simplify the derivation process, the following basic assumptions are made:

1. The contact behavior occurs only on the asperities, and the adjacent asperities are independent of each other;
2. The asperity is conical in shape, and the peak heights obey the Gaussian distribution near the mean value of the rough surface height;
3. The friction coefficient is regarded as the sum of adhesive component μ_a and furrow component μ_p,

$$\mu = \mu_a + \mu_p. \tag{1}$$

Adhesion component of friction coefficient

The adhesion component of friction f_a can be calculated as

$$f_a = \mu_a F_n, \tag{2}$$

where F_n is the normal load.

Based on the frictional mechanism of two rough surfaces (Fig. 3), we assume that the total contact points are N, and naturally F_n in Eq. (2) can be given as the sum of the ith product of the effective contact area $\bar{A}_{ri}$ and the normal compressive stress of the softer surface σ_i of the ith contact point,

$$F_n = \sum_{i=1}^{N} \bar{A}_{ri}\sigma_i. \tag{3}$$

According to Bowden and Tabor [17], the real contact area of two rough surfaces mainly happens on the peaks of asperities, and the contact area of each asperity gets more and more larger during the loading process. The larger deformation usually occurs on the asperities (with higher height) that have entered the contact state earlier, and eventually the normal compressive stress will reach the compressive strength of the softer surface, σ_y, causing the plastic deformation of the asperities. The plastic deformation of these asperities will continue to increase and subsequently more asperity will gradually enter the contact state, until the total stress of all the asperities is able to balance the external load. Therefore, the compressive stresses of the contact asperities with higher height and lower height are σ_y and σ_i, respectively, and the Eq. (3) can be derived as [18]

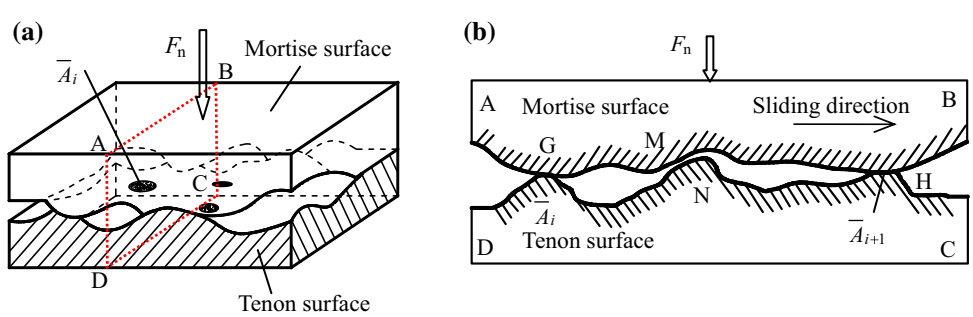

Fig. 3 Frictional mechanism of two solids with rough surfaces. **a** 3D contact state; **b** 2D contact state

$$F_n = \sigma_y \sum_{i=1}^{N_1} \bar{A}_{ri} + \sum_{i=1}^{N_2} \bar{A}_{rj}\sigma_i, \tag{4}$$

where $\overline{A}_{ri}$ and $\overline{A}_{rj}$ are, respectively, the contact area of a single contact asperity peak with higher height (plastic contact state) and lower height (elastic contact state). N_1 and N_2 are correspondingly the numbers of asperities with higher height and lower height, respectively.

The equilibrium morphology of a single asperity under such deformation state is shown in Fig. 4.

According to the relevant research, there usually exist large plasticity areas on the tenon surfaces at the later stage of loading. When the number of asperity in the plastic state is larger than that in the elastic state, the second item of Eq. (4) can be approximately ignored. In fact, the observation of the ratio of elastic region to plastic region is difficult to achieve and such bold assumption is made according to [18].Therefore, the Eq. (4) can be written as

$$F_n = \sigma_y A_r, \tag{5}$$

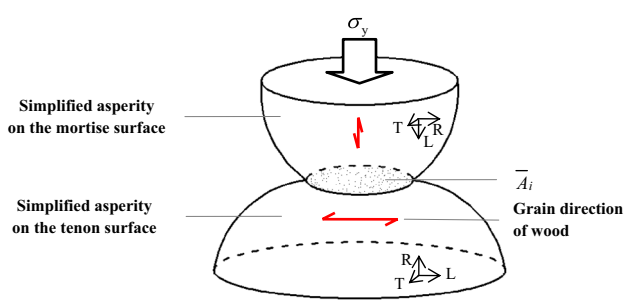

Fig. 4 Simplified contact model of single asperity under pressure. *L*, *R* and *T* denote the longitudinal, radial and tangential directions of wood, respectively

where A_r denotes the effective plastic contact area, sum of plastic contact areas of all individual asperities and can be given by

$$A_r = \sum_{i=1}^{N_1} \overline{A}_{ri}. \tag{6}$$

Considering the adhesive friction component f_a in the tangential direction, it equals the force needed to overcome the adhesion effect between the mortise and tenon surfaces, and can be expressed as

$$f_a = A_r \tau, \tag{7}$$

where τ is the shear strength of the softer surface.

With Eqs. (2), (5) and (7), the adhesion component of friction coefficient μ_a can be derived as

$$\mu_a = \tau/\sigma_y. \tag{8}$$

Generally, the value of σ_y is approximately equal to the surface hardness H of the softer rough surface [18]. This means that Eq. (8) can be calculated as

$$\mu_a = \tau/H. \tag{9}$$

Furrow component of friction coefficient

The furrow component of friction f_p can be calculated as

$$f_p = \overline{N}\sigma_y S, \tag{10}$$

where $\overline{N}$ represents the equivalent number of contact rough peaks and S is the ploughing area.

In the contact problems, the calculation of $\overline{N}$ and S of the furrow action usually needs the simplification of the contact asperities into conical rough peak, as shown in Fig. 5.

According to the assumption (2), the peak height obeys the Gaussian distribution. When establishing the rectangular coordinate system at the position of the mean roughness height, the height of rough peak z obeys standard

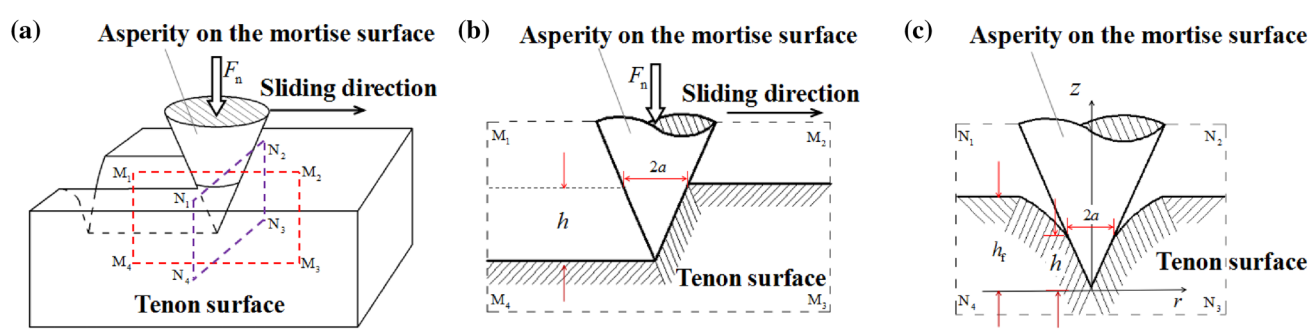

Fig. 5 Model of single asperity on mortise surface pressing semi space of tenon surface. **a** 3D view; **b** 2D view along the sliding direction; **c** 2D view perpendicular to the sliding direction

normal distribution, and the probability density $P_N(z)$ can be expressed as

$$P_N(z) = \frac{1}{\sqrt{2\pi}R_a} \exp\left[-\frac{z^2}{2R_a^2}\right], \tag{11}$$

where R_a is the surface roughness at the direction of ploughing.

Assuming the total number of the rough peaks is N_0, the number of the ones that occur in the interval $(z, z + dz)$ is $N_0 P_N(z)d(z)$. Fig. 5c shows the model that single conical rough peak pressing into the semi space. The relation between indentation depth h_f and contact radius a can be deduced as [19]

$$h_f = \frac{\pi}{2} a \tan\theta, \tag{12}$$

$$\theta = \arctan\left(\frac{2R_a}{RS_m}\right), \tag{13}$$

where θ is the complementary of the half cone angle and RS_m is the average width of the rough peaks at the ploughing direction.

If the height of the rough peak z is greater than the initial distance of two contact surfaces h_0, then the expression of the indentation depth h_f is

$$h_f = z - h_0. \tag{14}$$

Substituting Eq. (14) into Eq. (12), the expression of contact radius a can be deduced as

$$a = \frac{2(z - h_0)}{\pi \tan\theta}. \tag{15}$$

Therefore, the contact area of one single rough peak A_0 is

$$A_0 = \pi a^2 = \frac{4(z - h_0)^2}{\pi \tan^2\theta}. \tag{16}$$

By definition of Eq. (15), we can obtain the total number of the entire contact rough peak and their total contact area, which are expressed as Eqs. (17) and (18), respectively,

$$N = \int_{h_0}^{\infty} N_0 P_N(z) dz, \tag{17}$$

$$A = \int_{h_0}^{\infty} N_0 P_N(z) \frac{4(z - h_0)^2}{\pi \tan^2\theta} dz. \tag{18}$$

The average contact area and the equivalent number of contact rough peaks can be derived, respectively, as

$$\bar{A}_0 = \frac{\int_{h_0}^{\infty} N_0 P_N(z) \frac{4(z-h_0)^2}{\pi \tan^2\theta} dz}{\int_{h_0}^{\infty} N_0 P_N(z) dz}, \tag{19}$$

$$\bar{N} = \frac{A}{\bar{A}_0} = \frac{F_n}{H\bar{A}_0}, \tag{20}$$

The expressions of equivalent contact radius $\bar{a}$ and equivalent indentation depth $\bar{h}$ can be described as Eq. (21) and Eq. (22), respectively,

$$\bar{a} = \sqrt{\frac{\bar{A}_0}{\pi}}, \tag{21}$$

$$\bar{h} = \bar{a} \tan\theta. \tag{22}$$

Ploughing depth h_f' consists of equivalent indentation depth and the engaged depth, and it can be deduced as

$$h_f' = \bar{h} + R_a', \tag{23}$$

where R_a' is the surface roughness of the smoother surface of the two contact surfaces.

Therefore, the ploughing area is

$$S = a h_f'. \tag{24}$$

Combining with the equations from Eq. (20) to Eq. (24), the resistance due to the furrow action f_p can be derived as

$$f_p = \frac{F_n}{H\bar{A}_0} \sigma_y \left(\frac{\bar{A}_0}{\pi} \tan\theta + R_a' \sqrt{\frac{\bar{A}_0}{\pi}}\right). \tag{25}$$

Therefore, the furrow component of friction coefficient μ_p is

$$\mu_p = \frac{\sigma_y}{H\bar{A}_0} \left(\frac{\bar{A}_0}{\pi} \tan\theta + R_a' \sqrt{\frac{\bar{A}_0}{\pi}}\right). \tag{26}$$

In summary, the proposed friction coefficient model was expressed as

$$\mu = \frac{\tau}{H} + \frac{\sigma_y}{H\bar{A}_0} \left(\frac{\bar{A}_0}{\pi} \tan\theta + R_a' \sqrt{\frac{\bar{A}_0}{\pi}}\right). \tag{27}$$

Modification of friction coefficient model

The proposed friction coefficient model is independent of the relative sliding velocity and failed to model the relative sliding

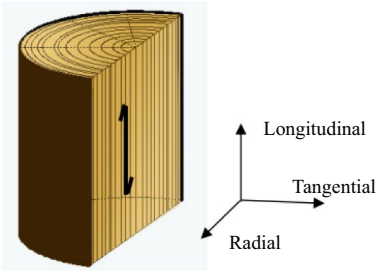

Fig. 6 Wood orientations. The black bidirectional arrow indicates the grain direction

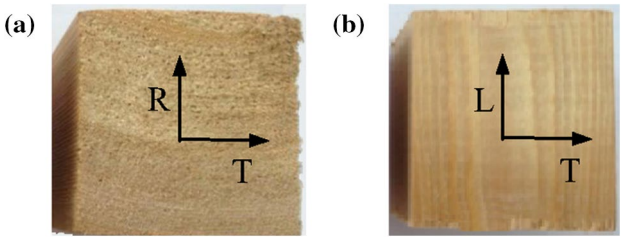

Fig. 7 Surface morphology of wood. **a** Transverse section and **b** tangential section

between the mortise and tenon during the pulling-out of tenon from mortise. Therefore, a modification was made by referring to [20],

$$\mu = \left[\frac{\tau}{H} + \frac{\sigma_y}{H\overline{A}_0}\left(\frac{\overline{A}_0}{\pi}\tan\theta + R'_a\sqrt{\frac{\overline{A}_0}{\pi}}\right)\right]\frac{2}{\pi}\arctan\left(\frac{v}{d}\right), \quad (28)$$

where v is the relative sliding velocity of mortise and tenon, and d is the critical relative sliding velocity.

Model parameter determination

Surface topography test

All the specimens were fabricated with the same batch wood from the same tree species with the frame tests. The material used was northeast larch of China and 15 clear samples without any defects such as knots, decay and cracks were made. Densities of these samples were 577 kg/m^3 and the average moisture content was 13.3%. The samples were prepared at three orientations, namely the longitudinal, the radial and the tangential directions (Fig. 6). The dimensions of all the samples in three directions were 50 mm (Fig. 7).

The surface topography of the samples was measured by the PS-50 type non-contact 3D surface topography instrument (Fig. 8), which consists of scanning system (test bench and optical measuring probe), acquisition and analysis system, and professional 3D analysis software. The scanning range of this instrument was 50 mm × 50 mm in x–y plane and 27 mm in the z direction with the scanning step 0.1 µm and resolution ratio 2 nm.

Table 1 shows the 3D topography of the transverse and tangential sections of one sample. It consists of the color map and the color height bar. Different colors clearly represent different surface features of the tested specimen surface, especially the height difference. The warmer colors, for example, red, represent the higher height, usually representing the profile peaks. The cooler colors, for example, blue, represent the lower height, usually representing the profile valley. The texture feature of wood materials in three

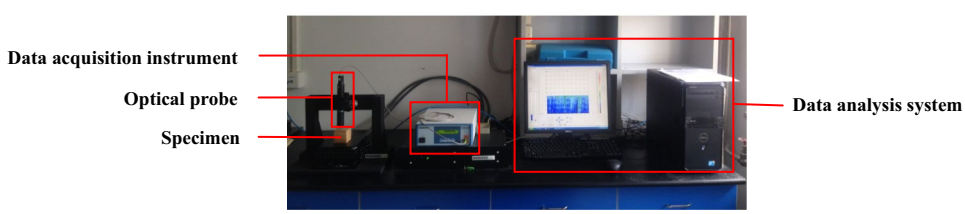

Fig. 8 PS-50 type non-contact 3D surface topography instruments

Table 1 3D topography of wood specimens

Surface	Transverse section	Tangential section
Topography	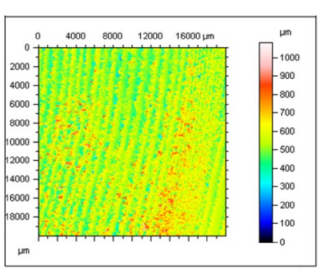	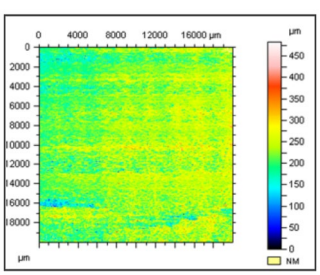

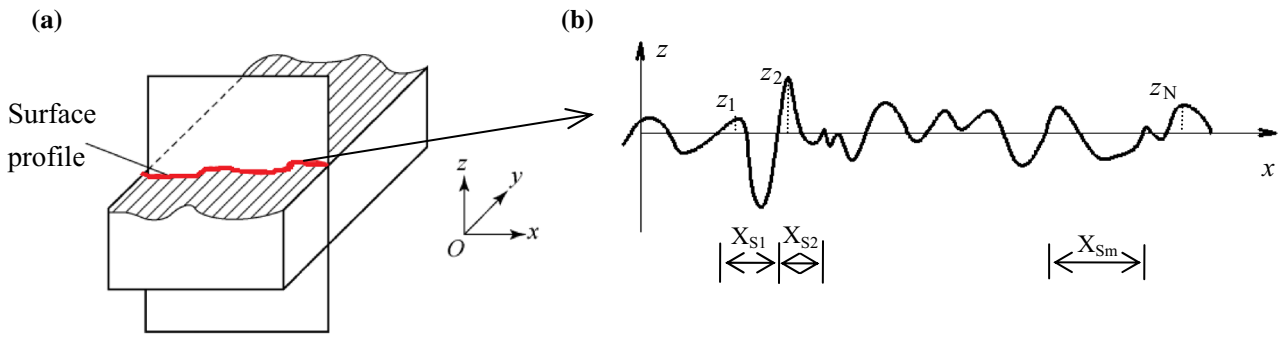

Fig. 9 Diagram of surface profile and the calculation method of the surface profile parameters. **a** Diagram of surface profile; **b** the calculation method of the surface profile parameters

orthogonal directions can also be seen. The annual rings in the transverse section are clearly visible, but are less obvious in the tangential section.

Surface profile parameters

Surface profile describes the intersection profile that a certain surface truncated the actual material surface (Fig. 9). The calculation method of surface profile parameters R_a and RS_m were given, as shown in Eqs. (29) to (31). Datum line is the contour line based on the method of least square method, which makes the sum of the squares of the distances from each point on the contour line to the datum line have minimum value. The computational formulae of the surface profile parameters are shown as follows:

$$R_a = \frac{1}{N}\sum_{i=1}^{N}|z_i|, \tag{29}$$

$$RS_m = \frac{1}{m}\sum_{i=1}^{m}X_{si}, \tag{30}$$

$$S_a = \frac{1}{MN}\sum_{j=1}^{N}\sum_{i=1}^{M}\left|\mu\left(x_i, y_i\right)\right|. \tag{31}$$

Based on the equation above, the results of the surface profile parameters are shown in the Table 2.

Surface hardness test

According to method of testing in hardness of wood (GB1941-91) [21], 20 samples were fabricated with the same batch wood from the same tree species as the frame tests. The dimensions of the samples are 75 mm × 50 mm × 50 mm with the 75 mm lying in the longitudinal direction. The hardness of two tangential surfaces and one transverse surface of each sample is tested, Fig. 10. The loading rate was 4 mm/min. The test terminated when the steel head of the hardness tester was pressed 5.64 mm into the tested surface.

The average surface hardness of wood in the transverse and tangential surface is 24.53 and 14.38 N/mm^2, respectively.

Table 2 Surface profile parameters

Surface direction	Parameters		
	S_a(μm)	R_a (L) (μm)	RS_m (L) (μm)
Transverse	63.27	–	–
Tangential	28.64	8.49	404.92

"L" represents the "Longitudinal" direction of wood specimens

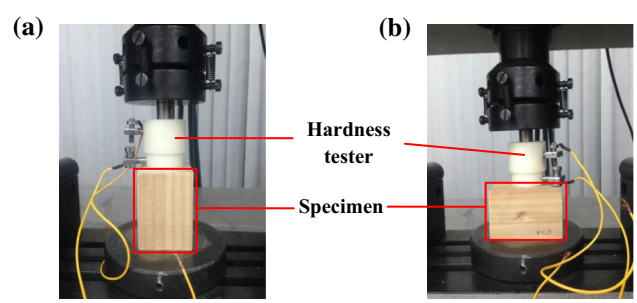

Fig. 10 Surface hardness of wood. **a** Transverse section; **b** tangential section

FE implementation of wooden frame with mortise and tenon joints

Finite element code ABAQUS was utilized to obtain numerical simulations of wooden frame with straight mortise and tenon joints [22]. The detailed dimensions of the FE model were shown in Fig. 11 and the established corresponding FE model is shown in Fig. 12. The elastic

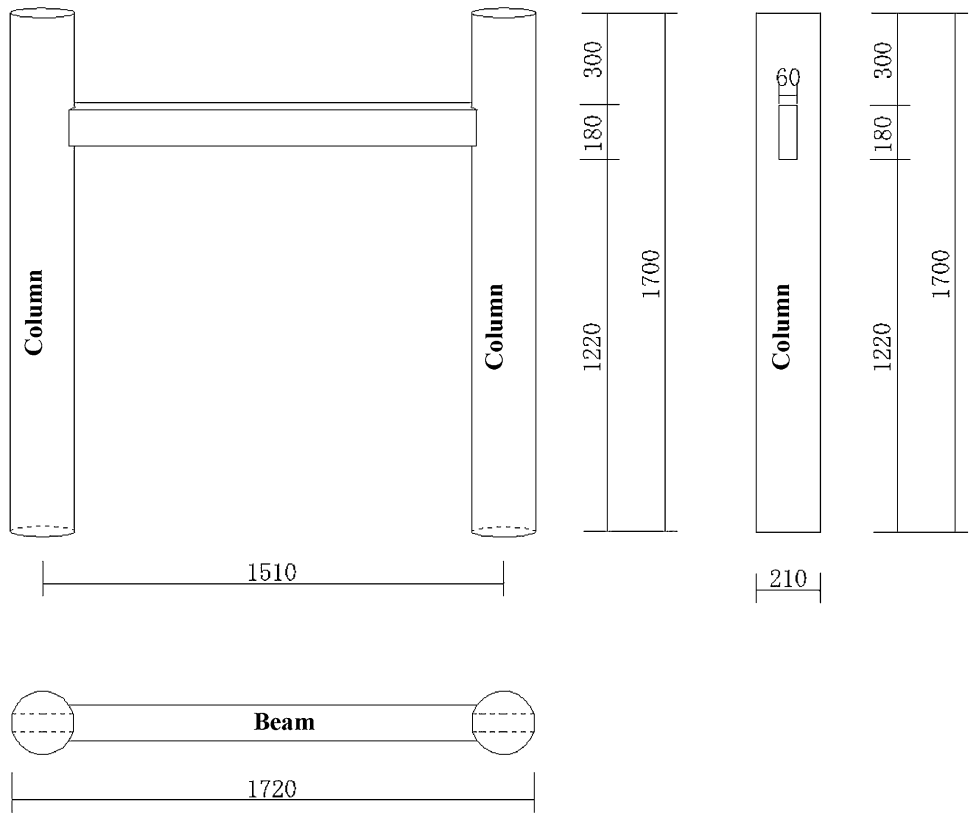

Fig. 11 Dimensions of the FE model (unit: mm)

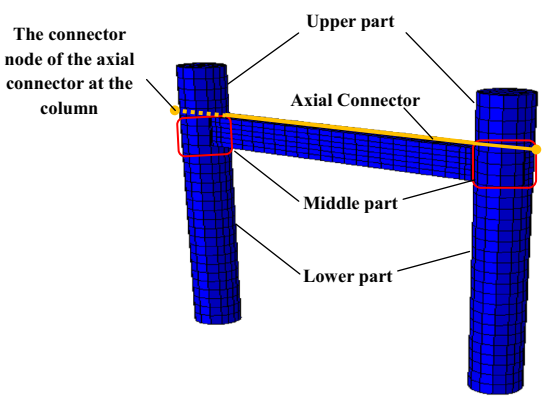

Fig. 12 Finite element model of timber frame

constants adopted to define the orthogonal characteristics of wood at the elastic stage were shown in Table 3. The plasticity compressive stress–strain relation parallel and perpendicular to grain, which were utilized to model the plastic behavior of the mortise and tenon, were respectively shown in Fig. 13a, b. The compressive strength of wood, parallel and perpendicular to grain, the hardening modulus of wood perpendicular to grain was also given in Table 3. As for annual ring direction for the beam section determining the embedment direction of tenon and affecting the FE analyses of joints, it seems that there exists several cases for such an issue due to anisotropic characteristic of wood; however, it is made as a deterministic issue by the sampling method of beam and tenon from a log. The annual ring direction for the sawn beam section and tenon section always goes along the radial direction. The column was hinged at the bottom. The vertical load 20 kN was applied on top of the column to simulate the loading boundary condition of the test, done by authors [23]. An axial connector whose modulus of elasticity was usually assigned a far bigger value than wood (such as 10^6) was used to keep the constraint conditions of the two joints approximately same with the experiment. The axial connector was assembled at the same height with the top

Table 3 Adopted material properties of the wood tested by the authors [25]

E_L (N/mm^2)	$E_R = E_T$ (N/mm^2)	$\mu_{LT} = \mu_{LR}$	μ_{RT}	$G_{LR} = G_{LT}$ (N/mm^2)	G_{RT} (N/mm^2)	σ_L (N/mm^2)	σ_R (N/mm^2)	E_{R2} (N/mm^2)
9124.52	716.13	0.346	0.499	700	300	46.83	7.0	70

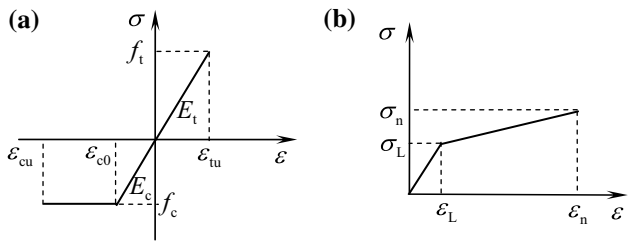

Fig. 13 Stress and strain relationship of wood. **a** Parallel to grain; **b** compression in radial direction

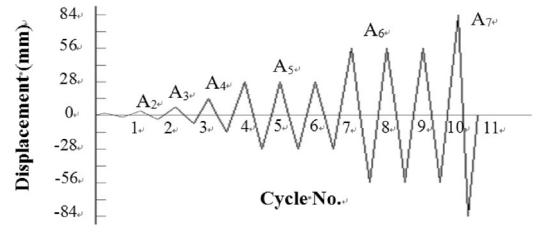

Fig. 14 Loading procedure adopted for the cyclic tests

surface of the beam connecting the column as shown in Fig. 13. The horizontal load was applied at the side of the column with the same height of the beam, where the actuator was positioned during the test process. The controlled lateral displacement amplitude for the wooden frames was shown in Table 4. For the first four loading amplitudes, one loading cycle was applied with each given displacement and three cycles for each loading amplitude of the later amplitudes. The schematic of the variable amplitude loading process controlled by displacement was shown in Fig. 14. The adopted model parameters were shown in Table 5. The C3D8R (8-node linear brick element, reduced integration with hourglass control) [24, 25] type element was used. The column was divided into three sections—the upper part, middle part and lower part (Fig. 12), with the mortise and tenon contact region as the boundary, to obtain a good FE mesh. The middle part was meshed with hexahedral elements, using the structured mesh technique. The other two parts were meshed with hex-dominated elements (primarily hexahedral elements, but allow some triangular prisms (wedges) in transition regions) using sweep technique. All the three parts of the column were meshed using the rectangular coordinate system.

Results and discussion

Hysteretic curve

Figure 15 shows the comparison of the simulation results with the friction model and constant friction coefficient $\mu = 0.5$, and the test result, which approximately shows good consistency.

The hysteresis curves from both the finite element simulations and the test result are shuttle-shaped, and pinching could be obviously observed. Sliding phenomenon is more and more obvious with the increase of displacement.

Using the established fiction constitutive model, the simulation result is able to better reflect the test result than the FE model with a constant friction coefficient in reflecting the "Necking" feature. Qualitatively, finite element results are relatively more closer to the experimental results when the displacement exceeded about 50 mm. To investigate the underlying causes of large errors existing in (− 50, 50) deformation intervals, each characteristic hysteresis loop was picked out from the hysteresis curve (Fig. 15) and analyzed separately as shown in the following parts.

Characteristic hysteresis loop analysis under controlled lateral displacement amplitudes A_1~A_7

The hysteresis loops at each controlled lateral displacement amplitude A_1~A_7 (Table 4; Fig. 14) are shown in Fig. 16a–g, the first three figures of which are, respectively, the first cycle of the three cycles obtained from the FE simulation and test results at each controlled lateral displacement amplitude of A_7, A_6 and A_5, and the others are, respectively, the unique load loops at A_4, A_3 A_2 and A_1.

The capability of the proposed friction model and the traditional constant friction coefficient model to reflect the experiment result is basically the same, coinciding with the test result when the displacement is greater than about 30 mm (Fig. 16a–c). However, when the displacement is less than about 15 mm (Fig. 16d–g), the experimental results are quite different from the simulation results, and the differences between the two FE models are very small. The cycles obtained from test result in Fig. 16c, d show strong

Table 4 The controlled displacement amplitude [25] (unit: mm)

	One loading cycle					Three loading cycles				
Amplitude	A_1	A_2	A_3	A_4	A_5	A_6	A_7	A_8	A_9	A_{10}
Value	1.76	3.53	7.05	14.1	28.2	56.4	84.6	112.8	141	169.2

Table 5 Model parameters

Surface contact pair	σ_y (N/mm^2)	τ (N/mm^2)	H (N/mm^2)	$\tan\theta$	R'_a (mm)	$\bar{A}$ (mm^2)	d (mm/s)	π
Ta–Ta	7.0	8.03	24.53	0.042	8.49	807,302	0.0005	3.14
Ta–Tr	4.68	8.03	24.53	0.042	8.49	864	0.0005	3.14

"Surface contact pair" represents the contact surface between the mortise and tenon; "Ta" is the abbreviation of "tangential" and "Tr" is the abbreviation of "transverse"

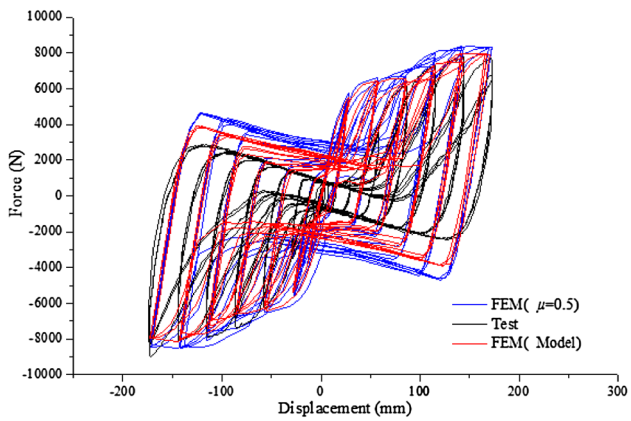

Fig. 15 The load–displacement hysteresis curve

asymmetry, and their reverse cycle tend to be more closer to the simulated result than the positive cycle. The reasons of all the above inconsistency lie mainly in the fabrication and installation errors of the test model, especially the initial gap between the mortise and the tenon, causing the smaller slope of the test result than the simulation result. When the displacement is less than 7.5 mm, the load–displacement curve obtained from FE model is approximately a straight line, which is due to the substantial recoverable deformation of the mortise and tenon.

Stiffness–displacement relationship

The stiffness of the frame obtained from the finite element model (FEM) with constant friction coefficient and using the proposed friction model was analyzed and they both were compared with the test result (shown in Fig. 17) to investigate the capacity of the FEM to reflect the test result during the first seven controlled lateral displacement amplitudes $A_1 \sim A_7$. The stiffness decreased sharply with the increasing of displacements during this interval when the displacement was less than 10 mm. During the (10, 50) deformation intervals, the stiffness obtained from the FE analysis was larger than that from the test result, which was mainly caused by the ignorance of the gaps between the mortise and tenon surfaces in the idealized finite element model. When the displacement exceeded 50 mm, the FE results were gradually converged.

Energy dissipation

According to the energy dissipation–displacement relationship of the FEM and test result shown in Fig. 18, when the displacement was less than 15 mm, the structural model using FE method basically does not consume the input energy due to the idealization of contact conditions between the mortise and tenon surfaces, indicating that the joint was in a state of elastic compression. The energy dissipation capacity of the FEM with constant friction coefficient was better than the one using the proposed fiction model during the displacement range 15–84.6 mm and the former coincided more closely with the test result.

As is seen from Figs. 16, 17 and 18, when displacement was less than about 50 mm, an approximate consistency agreement with the experimental results was obtained through the use of the proposed model. The relevant error may be derived mainly from three aspects: first, the assumption that the normal contact stress acts on the whole contact surface but not the real contact surface during the theoretical analysis (Eq. 4), which precisely resulted from the difficulties in determining the real contact surface during the cyclic loading. Therefore, the FE model result can better agree with the test result when the displacement exceeded 50 mm. Second, the dimensional errors in the specimens fabrication and the installation errors induced gap between the mortise and tenon surfaces also contributed to the resulted errors. Third, the ignorance of the cyclic loading induced smooth and slippy of wood surface, led to the overestimation of the simulation result than the experiment result during the whole loading process.

Conclusion

In this paper, a friction constitutive model for wood is presented and successfully implemented into the commercial ABAQUS software, via a user-defined subroutine. FE simulation of a Chinese ancient wooden frame with mortise–tenon joints under reversed cyclic loading was performed using the proposed friction constitutive model and a constant friction coefficient 0.5, respectively. The experimental results were used to validate the results of the two models, and better agreement of the proposed model was

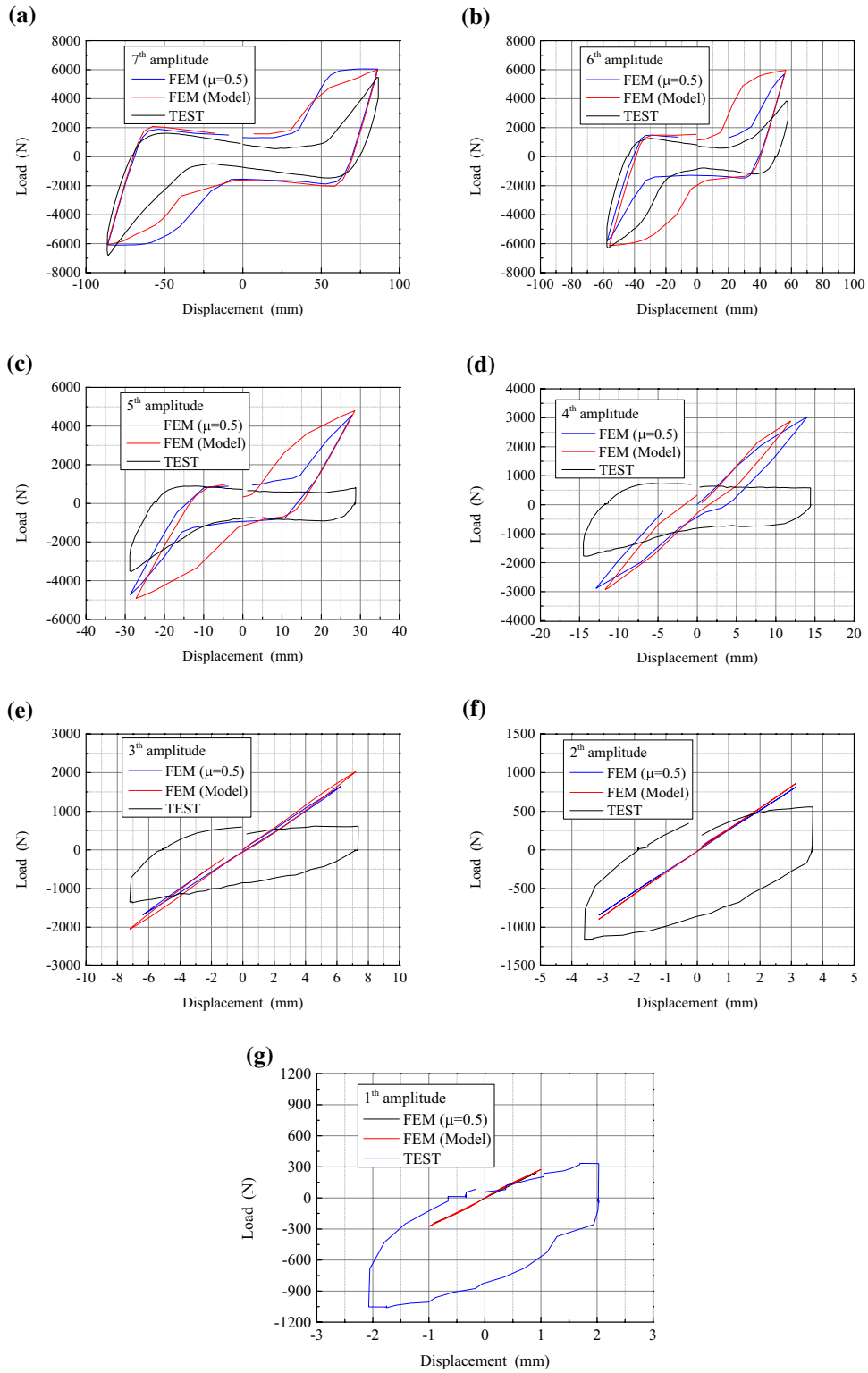

Fig. 16 Characteristic hysteresis analysis under controlled lateral displacement amplitudes

observed. The hysteresis curves obtained from the FE simulation based on the proposed model can better reflect the shuttle-shaped and pinching phenomena. When displacement was less than about 50 mm, the FE model result was an approximation to reflect the test results, and the model error mainly lie in the theoretical assumption that the normal contact stress acts on the whole contact surface but not on the real contact surface, the specimen fabrication and

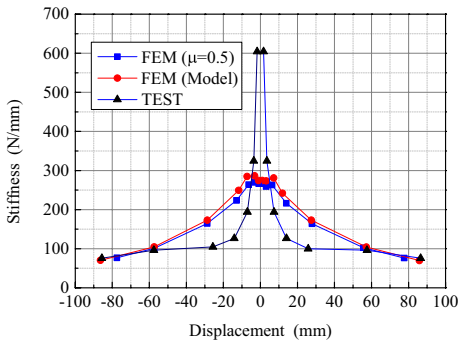

Fig. 17 Stiffness–displacement relationships

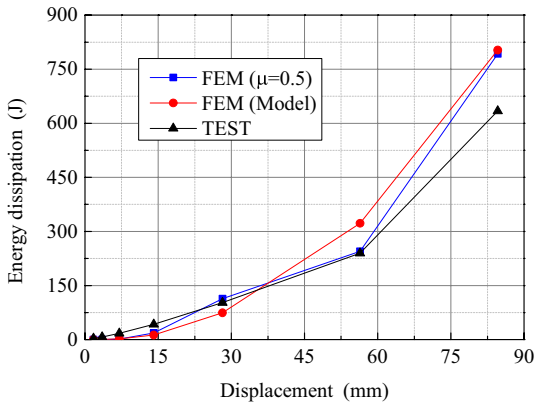

Fig. 18 Energy dissipation–displacement relationships

installation errors, and the ignorance of the cyclic loading induced smooth and slippery wood surface.

Acknowledgements The authors of this paper gratefully acknowledge the funding support received from the NSFC (Grant no. is 51278399) and Science and Technology Department of Shaanxi Province of China (Grant no. is 2016ZDJC-23).

References

1. Chen CC, Qiu HX, Lu Y (2016) Flexural behavior of timber dovetail mortise–tenon joints. Constr Build Mater 112:366–377
2. D'Ayala DF, Tsai PH (2008) Seismic vulnerability of historic Dieh–Dou timber structures in Taiwan. Eng Struct 30:2101–2113
3. Fang DP, Iwasaki S, Yu MH, Shen QP, Miyamoto Y, Hikosaka H (2001) Ancient Chinese timber architecture I: experimental study. J Struct Eng 11:1348–1357
4. Li J (1950) Yingzao Fashi (in Chinese). The Commercial Press (CP), China
5. Ma BJ (1991) Construction technology of Chinese ancient timber architectures. Science Press, China (**in Chinese**)
6. Wang T (1992) Static mechanics of ancient timber structures. Historical Relic Press, China (**in Chinese**)
7. Li XW, Zhao JH, Ma GW, Chen W (2015) Experimental study on the seismic performance of a double-span traditional timber frame. Eng Struct 98:141–150
8. Seo JM, Choi IK, Lee JR (1999) Static and cyclic behavior of wooden frames with tenon joints under lateral load. J Struct Eng 3:344–349
9. King WS, Yen JYR, Yen YNA (1996) Joint characteristics of traditional Chinese wooden frames. Eng Struct 18:635–644
10. Chun Q, Yue Z, Pan JW (2011) Experimental study on seismic characteristics of typical mortise–tenon joints of Chinese southern traditional timber frame buildings[J]. Sci Sin Techol 54(9):2404–2411
11. Derikvand D, Ebahimi G (2014) Strength performance of mortise and loose tenon furniture joints under uniaxial moment. J Forest Res-Jpn 25:483–486
12. Pan Y, Wang C, Tang LN, Li LJ (2015) Study on mechanical model of straight tenon joints in ancient timber structures (in Chinese). Eng Mech 32:82–89
13. Xie QF, Du B, Zhang FL, Zheng PJ, Xu QF (2014) Theoretical analysis on moment–rotation relationship of dovetail joints for Chinese ancient timber structure buildings (in Chinese). Eng Mech 12:140–146
14. Chang WS, Hsu MF, Komatsu K (2006) Rotational performance of traditional Nuki joints with gap I: theory and verification. J Wood Sci 52:58–62
15. Chang WS, Hsu MF (2007) Rotational performance of traditional Nuki joints with gap II: the behavior of butted Nuki joint and its comparison with continuous Nuki joint. J Wood Sci 53:401–407
16. Ogawa K, Sasaki Y, Yamasaki M (2016) Theoretical estimation of the mechanical performance of traditional mortise–tenon joint involving a gap. J Wood Sci 62:242–250
17. Bowen FP, Tabor D (1964) The friction and lubrication of solids. Oxford University Press, London
18. Liu ZM (2009) Tribology theory and design. Wuhan University of Technology Press, China
19. Sneddon IN (1965) The relation between load and penetration in the axisymmetric Boussinesq problem for a punch of arbitrary profile. Int J Eng Sci 3:47–57
20. Kobayashi S, Oh SI, Altan T, Chaudhary A (1990) Metal forming and the finite-element method. J Mater Shaping Technol 8:65–65
21. CRIWI GB1941-1991 (1992) Method of testing in hardness of wood (in Chinese). Research Institute of Wood Industry, Chinese Academy of Forestry, Beijing, p 59
22. Guan ZW, Zhu EC (2009) Finite element modelling of anisotropic elasto-plastic timber composite beams with openings. Eng Struct 31:394–403
23. Zhou WJ (2016) Experimental study on seismic behaviors of one-way straight mortise–tenon frames of ancient timber buildings. Dissertation, Xi'an University of Architecture and Technology, China
24. Chen ZY, Lu WZ, Zhu EC et al (2012) Structural performance of dougong brackets of yingxian wood pagoda under vertical load—refined finite element modelling. Sci Technol Eng 4:819–824
25. Dassault Systèmes Simulia Corp (2010) ABAQUS analysis user's manual Version 6.10. Providence, RI, USA